Nano Energy 57 (2019) 480–491

Contents lists available at ScienceDirect

Nano Energy

journal homepage: www.elsevier.com/locate/nanoen

Full paper

Data-driven and probabilistic learning of the process-structure-property relationship in solution-grown tellurene for optimized nanomanufacturing of high-performance nanoelectronics

Yixiu Wang[a,b], Raquel de Souza Borges Ferreira[c], Ruoxing Wang[a,b], Gang Qiu[d,e], Gaoda Li[a,f], Yong Qin[f,g], Peide D. Ye[d,e], Arman Sabbaghi[c,*], Wenzhuo Wu[a,b,e,h,**]

[a] School of Industrial Engineering, Purdue University, West Lafayette, IN 47907, USA
[b] Flex Laboratory, Purdue University, West Lafayette, IN 47907, USA
[c] Department of Statistics, Purdue University, West Lafayette, IN 47907, USA
[d] School of Electrical and Computer Engineering, Purdue University, West Lafayette, IN 47907, USA
[e] Birck Nanotechnology Center, Purdue University, West Lafayette, IN 47907, USA
[f] Institute of Nanoscience and Nanotechnology, School of Physical Science and Technology, Lanzhou University, Lanzhou, Gansu 730000, China
[g] School of Advanced Materials and Nanotechnology, Xidian University, Xi'an, Shaanxi 710071, China
[h] Regenstrief Center for Healthcare Engineering, Purdue University, West Lafayette, IN 47907, USA

ARTICLE INFO

Keywords:
Tellurene
Nanomanufacturing
Data-driven learning
2-D materials
Energy-efficient electronics
Process-structure-property relationship

ABSTRACT

Two-dimensional (2-D) semiconductors have been intensely explored as alternative channel materials for future generation ultra-scaled transistor technology [1–8]. However, significant roadblocks (e.g., poor carrier mobilities [9–11], instability [4,5,10], and vague potential in scaling-up [10,12–15]) exist that prevent the realization of the current state-of-the-art 2-D materials' potential for energy-efficient electronics. The emergent solution-grown tellurene exhibits attractive attributes, e.g., high room-temperature mobility, large on-state current density, air-stability, and tunable material properties through a low-cost, scalable process, to tackle these challenges [16]. Nevertheless, the fundamental manufacturing science of the hydrothermal processing for tellurene remains elusive. Here, we report on the first systematic, data-driven learning of the process-structure-property relationship in solution-grown tellurene, revealing the process factors' effects on tellurene's production yield, dimensions, and transistor-relevant properties, through a holistic approach integrating both the experimental explorations and data analytics. We further demonstrate the application of such fundamental knowledge for developing tellurene transistors with optimized and reliable performance, which can enable the cost-effective realization of high-speed, energy-efficient electronics.

1. Introduction

The economical production and integration of nanostructured semiconductors with designer properties are expected to provide exciting opportunities in the cost-effective realization of high-performance, energy-efficient electronics for emerging technologies [4,9,10,17–34], e.g., pervasive computing, wireless communication, and the Internet of Things (IoT). Atomically-thin 2-D layered van der Waals (vdW) materials, e.g., graphene, transition metal dichalcogenides, and black phosphorus, have been intensely explored as alternative channel materials for future generation ultra-scaled transistor technology that can meet the above application needs [1–5,9,35–37]. However, current state-of-the-art approaches for deriving 2-D materials through exfoliation of bulk materials [5,31] or bottom-up syntheses [33,38] show the limited potential of economically viable manufacturing and integration for practical technologies, largely due to restrictions in the growth conditions [10,12–15], small sizes [39], or instability [4,5,10] of the obtained materials. Feasible synthetic strategies for the scalable, substrate-free production of large-area 2-D crystals with designer and process-controlled properties are currently lacking [40]. Reducing manufacturing and integration costs while continuously improving device- and system-level performances remains a major challenge for existing nanotechnologies, which may be addressed through innovations in the design, processing, and integration of novel

* Corresponding author.
** Corresponding author at: School of Industrial Engineering, Purdue University, West Lafayette, IN 47907, USA.
E-mail addresses: sabbaghi@purdue.edu (A. Sabbaghi), wenzhuowu@purdue.edu (W. Wu).

https://doi.org/10.1016/j.nanoen.2018.12.065
Received 4 December 2018; Received in revised form 19 December 2018; Accepted 19 December 2018
Available online 25 December 2018

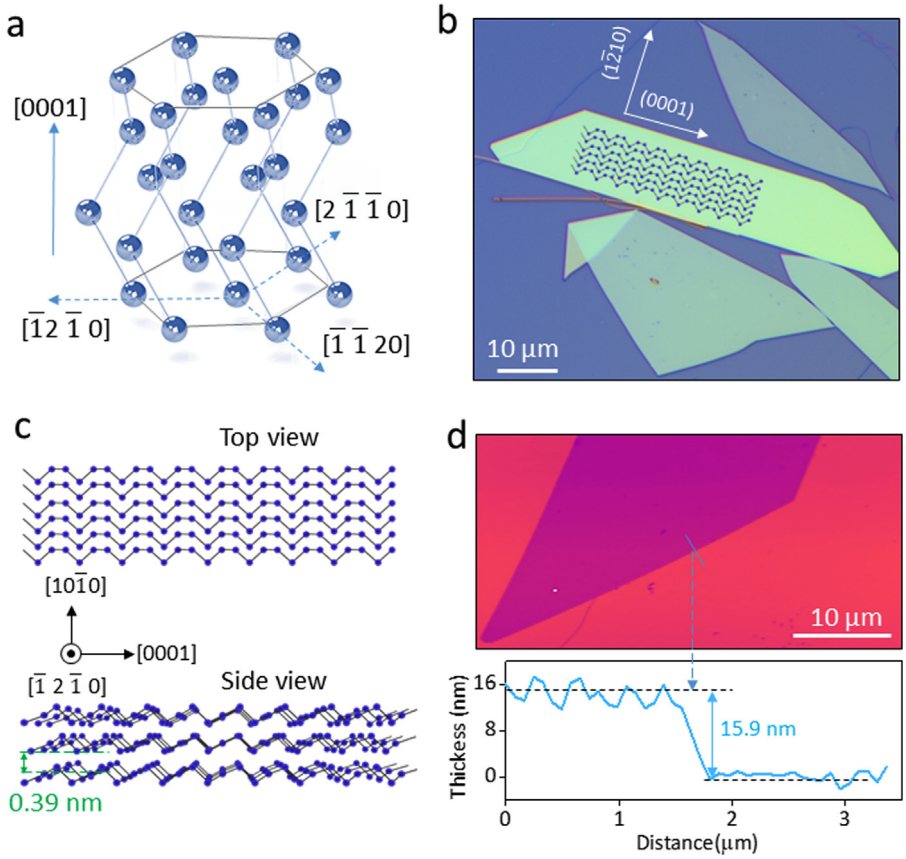

Fig. 1. Characterization of 2-D Tellurene. (a) The crystal structure of tellurium. (b) Optical image of the as-synthesized 2-D tellurene. The scale bar is 10 µm. (c) 3D illustration of 2-D tellurene's structure. (d) AFM image of a typical 2-D tellurene flake. The scale bar is 10 µm.

materials and device structures.

We recently reported a hydrothermal process that can achieve both high productivity and high quality for the scalable synthesis of a new 2-D semiconductor: tellurene, which is the 2-D form of elemental tellurium (Te) [16,41]. In contrast to the layered vdW 2-D materials, tellurene has a unique chiral-chain structure in which individual helical chains of Te atoms are stacked together by weak bonding, and the intra-chain interaction between neighboring Te atoms is covalent-type (Fig. 1a) [42–44]. Solution-grown tellurene has high room-temperature carrier mobility (~700 cm^2/Vs) [16], superior on-state current density (larger than 1000 mA/mm) [16], process-tunable bandgap (~0.35–1.2 eV from mid-IR to visible light) [16,43], and excellent air-stability [16], which are all promising for high-speed, low-power electronic systems. Tellurene also possesses other intriguing properties that are attractive for electronics and optoelectronics [16,45–50]. Moreover, the demonstrated hydrothermal process [16] exhibits several advantages over other state-of-the-art approaches concerning improved flexibility, productivity, and quality of manufacturing, as well as the integration of large-area crystalline 2-D materials into a device assembly. However, the fundamental nature and manufacturing science of the hydrothermal process for tellurene remain elusive. In particular, a more profound understanding of the process factors' effects on the outcomes of tellurene production is required to establish an optimized and reliable synthesis protocol for the large-scale production and application of tellurene materials.

Here, we report on the first systematic study and data-driven learning of the effects of essential process factors on production yield, dimensions, and physical properties of the as-synthesized tellurene, through a holistic and synergistic integration of both experimental explorations and statistical analyses. We focus on revealing the roles of the crystal-face-blocking ligand polyvinylpyrrolidone (PVP). Although previous results suggest that the initial concentration of PVP has a significant impact on the formation and dimension control of tellurene [16], a more detailed understanding of the interaction between PVP and the formed tellurene crystals is lacking. Ultimately, the knowledge obtained from our study is critical because these process factors directly impact growth rate, assembly yield, performance uniformity, and batch-to-batch reproducibility, which are important for modeling, design, manufacturing, integration, and optimization of 2-D tellurene-based technologies.

2. Results and discussion

2.1. Synthesis of tellurene with productivity and dimension control

A hydrothermal processing scheme similar to the reported procedure [16] was carried out to prepare the 2-D tellurene for this study. Specifically, sodium tellurite (Na_2TeO_3) was reduced by hydrazine hydrate (N_2H_4) in an alkaline solution at temperatures from 160 to 200 °C with the use of PVP (see Methods). The typical 2-D Te crystals possess lateral sizes from tens of µm to 100 µm (Fig. 1a), and crystallographic orientations are illustrated by the top-view 3D image overlaid on the optical image [16] (Fig. 1b). The tellurene crystals stack vertically along the [10$\bar{1}$0] direction and laterally along the [0001] and [$\bar{1}$2$\bar{1}$0] directions (Fig. 1c). The atomic-thin nature of the tellurene flakes is verified with the atomic force microscopy (AFM) characterization (Fig. 1d).

To learn the effects of PVP characteristics (e.g., molecular weight) on the growth outcome, a series of processes was performed with controlled conditions (e.g., specified mass ratios between Na_2TeO_3 and PVP, PVP molecular weights, and reaction times). As suggested by previous production studies, all processes were carried out at 180 °C

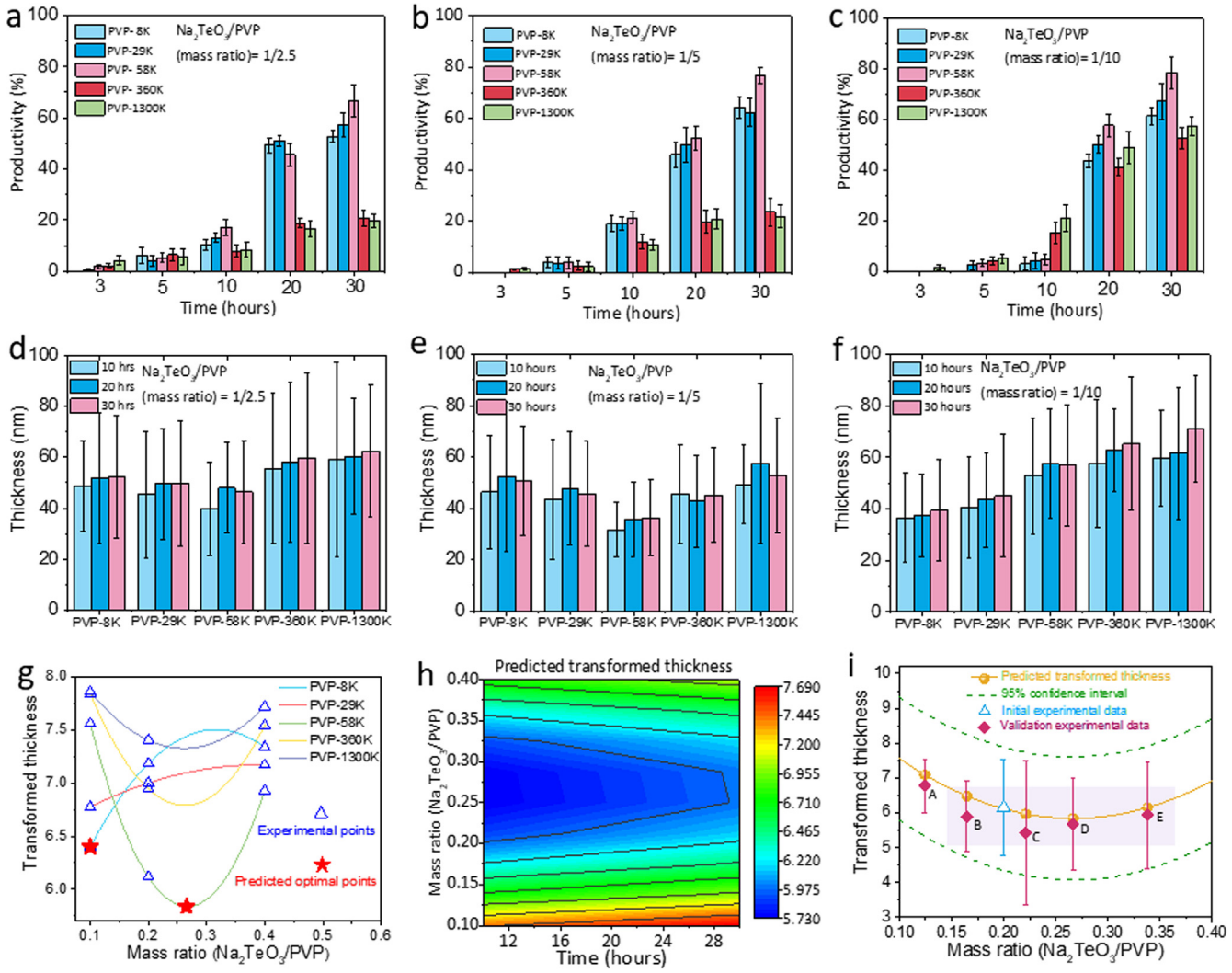

Fig. 2. Data-driven learning of 2-D tellurene synthesis with validation and optimization. (**a–c**) Growth outcome for different Na_2TeO_3/PVP mass ratios and PVP chain lengths. The average values from 8 technical replicates are indicated, and error bars represent one standard deviation for each set of replicates. (**d–f**) Thickness modulation of 2-D tellurene. The average values from 8 technical replicates are indicated, and error bars represent one standard deviation for each set of replicates. (**g**) An illustration of the predictions for the transformed thickness under different PVP chain lengths and Na_2TeO_3/PVP mass ratios as obtained from Eq. (3) for a fixed synthesis time (20 h). (**h**) An illustration of the predictions for the transformed thickness under different reaction time and Na_2TeO_3/PVP mass ratios for a fixed PVP chain length(58K). (**i**) Predicted thickness, initial experimental and new validation experimental results of 2-D tellurene thickness using Na_2TeO_3/PVP mass ratio, with PVP chain length fixed at PVP-58K for 20 h reaction. The average values from 8 technical replicates are indicated, and error bars represent one standard deviation for each set of replicates.

[16]. The PVPs with higher molecular weights possess longer polymer chain lengths [51] (Supplementary Table 1). As such, we will use the PVP chain length and molecular weight terms interchangeably throughout the remainder of our discussion. Fig. 2a–c plot the productivity (see Methods) of the tellurene nanostructures across time for three different Na_2TeO_3/PVP mass ratios and a broad range of PVP molecular weights. A morphology evolution with time in the synthesis products from 1-D structures to 2-D forms, similar to the reported results [16], occurs for all processes (Fig. 2a–c, Supplementary Figs. S1–3). Specifically, the productivity of the tellurene flakes increases with a reduction in 1-D and intermediate structures (Supplementary Fig. S1) and reaches a plateau after an extended growth, e.g., ~30 h (Fig. 2a–c, Supplementary Figs. S1–3). For constant Na_2TeO_3/PVP mass ratio (Fig. 2a–c, respectively), the first tellurene nanostructures emerge after a shorter reaction time when PVP with larger molecular weight is used (Supplementary Fig. S1). Nevertheless, the final productivities (after 20–30 h reaction) of tellurene for processes using PVPs with larger molecular weights (i.e., PVP-360K and PVP-1300K) are smaller than those for processes using PVPs with smaller molecular weights (PVP-8K, PVP-29K, and PVP-58K). When the PVP concentration increases (from Fig. 2a to b to c), the reaction time for the first tellurene nanostructures to appear increases for all processes. When the Na_2TeO_3/PVP mass ratio is 1/10 (Fig. 2c) the final productivity of tellurene for processes using PVPs with larger molecular weights increase considerably to ~50–60%, in contrast to the final productivities for processes using lower concentrations of the same PVPs that saturate at ~20% (Fig. 2a and b). Also, for all PVP concentrations, the processes using mid-range PVP molecular weights (i.e., PVP-58K) have the highest final productivity (Fig. 2a–c). Formal verifications of these observations follow from the statistical analyses performed in the next section.

The thickness and width of tellurene can also be effectively modulated by controlling the Na_2TeO_3/PVP mass ratio, growth time, and PVP molecular weight (Fig. 2d–f, Supplementary Fig. S4). We focus our discussion here on processes with sufficient reaction time that yield reasonable productivity (e.g., 10 h and beyond in Fig. 2a–c). We first study the thickness modulation. For low and medium PVP concentrations (alternatively, Na_2TeO_3/PVP mass ratios of 1/2.5 and 1/5 in

Fig. 2d–e), tellurene thickness appears to be minimized under the medium PVP molecular weight of PVP-58K (Fig. 2d–e). In contrast, for the high PVP concentration (alternatively, the Na_2TeO_3/PVP mass ratio of 1/10), tellurene thickness appears to monotonically increase with the PVP molecular weight (Fig. 2f). The growth time appears to have little effect on tellurene thickness in any process. Regarding width modulation, the tellurene width in any process appears to be maximized under PVP-58K (Supplementary Fig. S4). The processes using larger PVP molecular weights (i.e., PVP-360K and PVP-1300K) tend to yield the narrowest tellurene flakes among all groups. For a constant PVP molecular weight, tellurene width appears to be maximized under a medium PVP concentration (i.e., the Na_2TeO_3/PVP mass ratio of 1/5) (Supplementary Figs. S1–S3). The processes using a high PVP concentration (i.e., the Na_2TeO_3/PVP mass ratio of 1/10) give rise to the narrowest tellurene flakes among all groups. In contrast to the case of thickness modulation, reaction time has a more profound effect on width variation, with longer growth time leading to larger tellurene flake widths in all processes, which saturate after a reaction time of 20 h. All of these observations are verified by our statistical analyses in the next section.

2.2. Data-driven learning of the process factors' effects on 2-D Te synthesis

To obtain more formal insights into the fundamental mechanisms of 2-D Te synthesis, we carried out systematic, data-driven studies using advanced statistical methodologies. The summary of our results in this section demonstrates how our statistical approach can enable the learning of the effects of different process factors (e.g., PVP molecular weight, PVP concentration, and growth time) on productivity and dimension in tellurene production. Our results can further identify the process factors' settings that can optimize productivity and dimension in expectation, and yield minimum variability. In our data analyses, we separate dimension control into thickness and width control. The experiments involve different PVP concentrations and molecular weights, with synthesis time fixed at 20 h.

We first present the productivity analysis. As the raw productivity measurements lie between 0 and 1, we applied the logistic transformation (abbreviated as logit) to them. Specifically, the logistic transformation for an observation p (where $0 < p < 1$) is $\text{logit}(p) = \ln\left(\frac{p}{1-p}\right)$. Two separate linear regression models were fit to study the process factors' effects on the expectation and variability of the transformed productivity. Details on linear regression modeling can be found in the Supporting Methods. The fitted weighted linear regression model [52] for the expectation is

$$\begin{aligned}\hat{w} = &-5.3\times10^{-1}+2.9 \quad x_M - 4.2 \quad x_M^2 + I_{PVP-29K}(6.8\times10^{-1} - 4.2 \quad x_M + 7.9x_M^2)\\ &+ I_{PVP-58K}(1.2 - 5.1 \quad x_M + 4.2 \quad x_M^2)\\ &+ I_{PVP-360K}(1.7 - 20.9 \quad x_M + 33 \quad x_M^2)\\ &+ I_{PVP-1300K}(3.1 - 32.3 \quad x_M + 51.4 \quad x_M^2)\end{aligned} \tag{1}$$

where $\hat{w}$ denotes the predicted logit of productivity, x_M is the Na_2TeO_3/PVP mass ratio, and I_{PVP-i} is the indicator variable for PVP chain length i. Note that the indicator I_{PVP-8k} is omitted from this equation in accordance with the standard practice for preventing overparameterization in the regression model [52,53]. In this case, the predictions for PVP-8K are obtained by setting $I_{PVP-29K} = I_{PVP-58K} = I_{PVP-360K} = I_{PVP-1300K} = 0$ in Eq. (1). The fitted model for the standard deviation is

$$\hat{\sigma}_w = 2.2 \times 10^{-2} + 1.3 \quad x_M - 2.9 \quad x_M^2, \tag{2}$$

where $\hat{\sigma}_w$ is the estimated standard deviation of the transformed productivity for the Na_2TeO_3/PVP mass ratio x_M. Supplementary Fig. S5 illustrates the fitted model for the expected transformed productivity in Eq. (1). This figure immediately indicates two possible settings that can potentially enable the production of 2-D Te with desired productivity in expectation: (a) PVP-58K with medium-to-high PVP mole ratio concentration (corresponding to the Na_2TeO_3/PVP mass ratio of 1/5–1/10), denoted by the green line, and (b) PVP-1300K with high PVP mole ratio (corresponding to the Na_2TeO_3/PVP mass ratio of 1/10), denoted by the light purple line. The first setting yields the highest predicted transformed thickness over the given range of mass ratios. Also, PVP-1300K has an increasing positive trend in productivity as a function of mole ratio that suggests the transformed thicknesses can continue to increase, and potentially surpass the maximum thickness for PVP-58K, under mass ratios smaller than 1/10. In addition, we observe a quadratic effect of the Na_2TeO_3/PVP mass ratio for both of the models in Eqs. (1) and (2), which also indicates the existence of a maximum.

We next analyze 2-D tellurene thickness. The target thickness for functional devices (e.g., field-effect transistors) is ~10 nanometers as per previously shown data [16]. Thus, it is desired to identify the process factors' settings that both center tellurene thickness close to 10 nm and minimize its variability. To accomplish these two objectives, we transform tellurene thickness as $t = \ln((y-10)^2)$, and identify the process factor settings that minimize the transformed thickness t. This approach will enable the optimization of the combination of both expectation and variability of thickness [53]. The convenience offered by the transformation is further discussed in the Supporting methods. The fitted regression model is

$$\begin{aligned}\hat{t} = &4.9 + 1.3 \quad \times10^{-2}x_T + 14.9 \quad x_M - 23.5 \quad x_M^2\\ &+ I_{PVP-29K}(1.3 - 11.2x_M + 18.75 \quad x_M^2)\\ &+ I_{PVP-58K}(5.1 - 47.7 \quad x_M + 85 \quad x_M^2)\\ &+ I_{PVP-360K}(4.4 - 35.8x_M + 63.3 \quad x_M^2)\\ &+ \quad I_{PVP-1300K}(3.6 - 25.5 \quad x_M + 43.9 \quad x_M^2)\end{aligned} \tag{3}$$

where x_T denotes synthesis time. Fig. 2g illustrates the results for a synthesis time of 20 h, and suggests two factor settings that could potentially achieve the desired thickness in expectation with small variability: (a) high PVP concentration (corresponding to the Na_2TeO_3/PVP mass ratio of 1/10) with PVP-8K, denoted by the star symbol on the light blue line, and (b) medium PVP concentration (corresponding to the Na_2TeO_3/PVP mass ratio of 0.26667) with PVP-58K, denoted by star symbol on the green line. As previously discussed, the first scenario yields poor productivity in expectation. It should be noted that the second scenario is a "virtual" condition predicted by our analysis, which can illuminate the design of further validation and optimization experiments for identifying the optimal conditions. From these observations, we fix the chain length to PVP-58K and further investigate the effects of Na_2TeO_3/PVP mass ratio and growth time on transformed thickness. The results are demonstrated by the contour plot in Fig. 2h, suggesting that the transformed thickness can be minimized by using medium PVP concentration range (indicated by the color gradient on the contour plot) and a time of 20 h. Note that although shorter time (e.g., 12 h on the contour) suggest smaller transformed thickness, such short reaction period is not feasible in the context for 2-D tellurene production due to the low productivity (see Fig. 2a–c). Moreover, the transformed thickness is predicted to increase as a function of time for all Na_2TeO_3/PVP mass ratios.

To validate the above findings predicted by our formal analysis, we carry out additional syntheses following the predicted optimal conditions, as shown by the solid orange line in Fig. 2i that plots the mean of transformed thickness when the combined conditions of PVP-58K, 20 h reaction are used. It should be noted that the thickness values derived from these conditions (surrounding the predicted optimal point for the Na_2TeO_3/PVP mass ratio of 0.26667, at point D in Fig. 2i) show indistinguishably small differences (< 1 nm, Supplementary Table S2). This suggests the existence of an optimal PVP concentration range, instead of a single value, for our synthesis. To this end, we define a targeted mean transformed thickness of 5.89 to validate the model

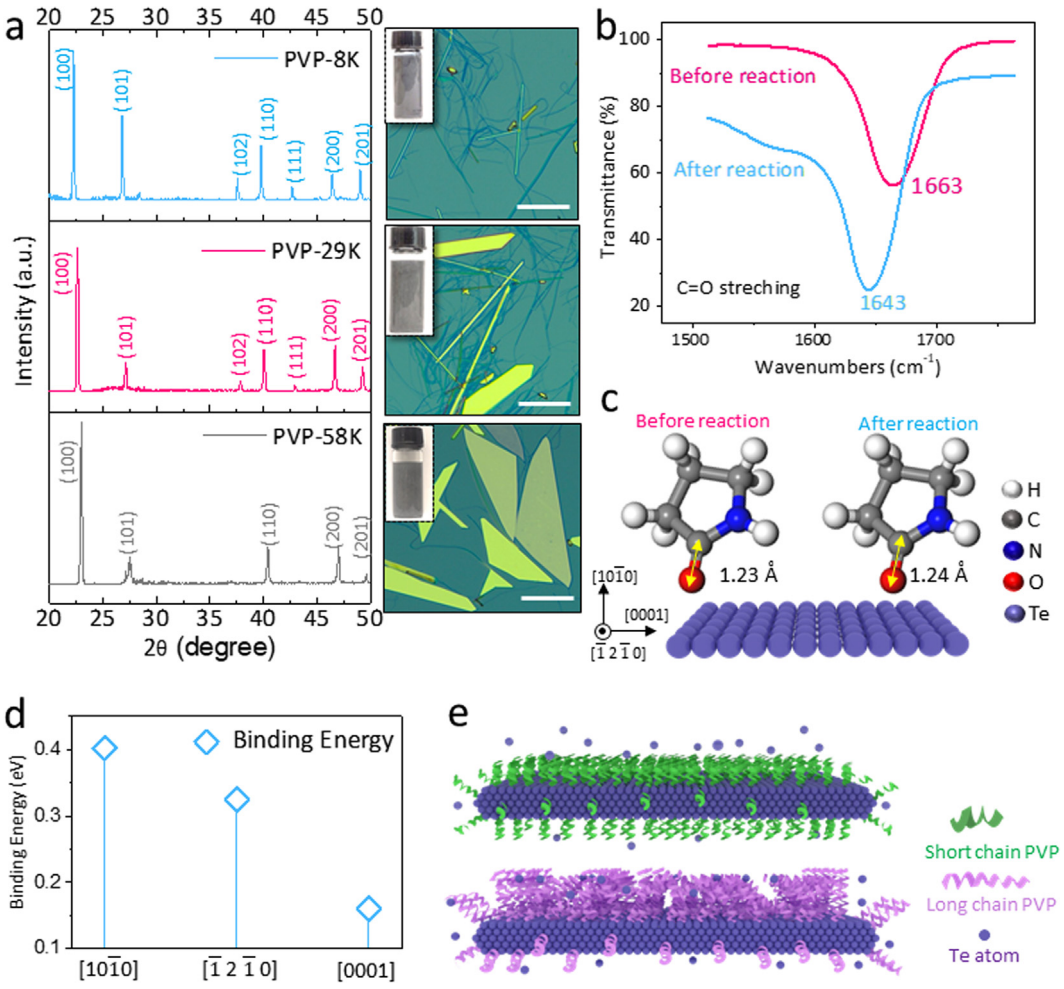

Fig. 3. Characterization of 2-D tellurene and DFT calculation of PVP binding with 2-D tellurene. (**a**) XRD pattern and optical image of 2-D tellurene for different PVP chain length reactions. The scale bar is 10 μm. (**b**) FTIR spectra of PVP before and after reaction. (**c**) DFT calculation of C=O bond length of PVP before and after reaction. (**d**) DFT calculation of binding energy between PVP and 2-D tellurene. (**e**) Scheme of the PVP configuration on 2-D tellurene with short and long chain length PVP.

presented in Fig. 2g and i, and the feasibility of the proposed range of optimal conditions (highlighted by the light purple area in Fig. 2i, Methods). Here, the value of 5.89 is the predicted minimum transformed thickness from our model in Eq. (3). Five conditions with Na_2TeO_3/PVP mass ratios of 0.12448 (A), 0.16480 (B), 0.22125 (C), 0.26667 (D), and 0.33793 (E) were adopted for the heuristic validation experiments, where conditions B, C, and E are predicted to yield a mean transformed thickness falling within one standard deviation from the targeted value, and condition A is predicted to generate a mean transformed thickness larger than one standard deviation from the targeted value. Here, one standard deviation for transformed thickness is 0.88 based on our model (Methods). All three synthesis procedures followed the steps described above using PVP-58K, with the statistical results shown in Fig. 2i (Methods). It can be seen that all experimental results agree well with the model predictions. The formal one-sample *t*-test of the results (Methods) from the validation experiment demonstrates that there is not a statistically significant difference between the mean transformed thickness at the mass ratio level of 0.26667 (point D) obtained from the validation experiment and the predicted value of 5.89 (*p-value* = 0.6567). Furthermore, additional two-sample *t*-tests (Methods) for the mass ratio levels of 0.26667 and 0.2 do not indicate any statistically significant differences on either the transformed (*p-value* = 0.5068) or original (*p-value* = 0.4543) thickness scales. The demonstrated close-loop cycle in the nanomanufacturing of tellurene exemplifies the capability and potential of our approach for extracting and uncovering fundamental synthesis knowledge through the learning of a limited amount of initial experiments (3 sets of conditions for each PVP case as shown in Fig. 2g), and generating valuable insights for guiding the design and optimization of the nanomanufacturing process.

Finally, we learn the effects of PVP concentration and molecular weights on the expectation and variance of 2-D Te width. As in our first analysis on productivity, we fit weighted linear regression models [52] to account for non-constant variance in 2-D Te width. Our fitted models are

$$\hat{z} = -1.3 + 73.2x_M - 120.8\ \ x_M^2 + \ \ I_{PVP=29K}(3.6 - 5.5x_M) + I_{PVP=58K}(6.9 - 4.1x_M) + I_{PVP=360K}(4.3 - 24\ \ x_M) + \ \ I_{PVP=1300K}(-1.7\times10^{-1} - 14.6\ \ x_M) \quad (4)$$

$$\hat{\sigma_z} = -6.8\ \ \times10^{-1} + 37\ \ x_M - 71.6\ \ x_M^2 + I_{PVP=29K}(3.1\times10^{-1} - 17.6x_M^2) + I_{PVP=58K}(2.1 + 12.2\ \ x_M^2) + I_{PVP=360K}(1.3\ \ \times10^{-1} - 4.3\ \ x_M^2) + \ \ I_{PVP=1300K}(-7.9\times10^{-1} - 6.4\ \ x_M^2) \quad (5)$$

where $\hat{z}$ denotes the predicted width and σ_z the estimated standard deviation for width. Similar to our results on productivity, the models in Eqs. (4) and (5) (which are illustrated in Supplementary Fig. 4d-e) indicate that PVP-58K with medium PVP concentration (corresponding to the Na_2TeO_3/PVP mass ratio of 1/5) will optimize width in expectation.

Our data-driven approaches indicate that the combination of a 20-h

synthesis, intermediate PVP concentration, and PVP-58K yield satisfactory results for productivity and dimension control of tellurene in expectation. Furthermore, they indicate that this combination also increases the variabilities of productivity and width. Thus, although our analyses do not conclusively identify factor settings that can simultaneously optimize productivity and dimension control of tellurene in terms of both expectation and variance, they do certainly illuminate those settings that merit further experimentation, and highlight the importance of new experiments involving more factors and measurements of desired properties for all types of experiments involving different factor setting combinations.

2.3. Mechanism exploration of 2-D Te synthesis

We further explore the effects of PVP characteristics on the formation of 2-D Te through material and structural characterizations. Fig. 3a and Supplementary Fig. S6 shows the X-ray diffraction (XRD) patterns of the 2-D Te samples after a 20-h reaction with a Na_2TeO_3/PVP mass ratio of 1/5 and using PVP-8K, PVP-29K, PVP-58K, PVP-360K, and PVP-1300K which yield relatively wide 2-D Te flakes with reasonable productivities (Fig. 2a-c). To identify the preferential crystal orientation in the 2-D Te samples and compare the morphology difference among the three groups, we assembled the as-synthesized 2-D Te crystals on the silicon wafer into Langmuir–Blodgett (LB) monolayer thin films [16]. All of the diffraction peaks seen in the three XRD patterns can be indexed to the trigonal Te phase. Specifically, the strong (100) peaks in all three XRD patterns indicate that the 2-D Te surfaces are dominated by the $\{10\bar{1}0\}$ planes, consistent with our TEM results [16]. The (102) and (111) peaks appear in the XRD patterns for samples synthesized using the small (PVP-8K, PVP-29K, Fig. 3a) and large (PVP-360K, PVP-1300K, Supplementary Fig. S6) molecular-weight PVPs, while these peaks are weak in the diffraction patterns for samples synthesized using the medium molecular-weight PVP (PVP-58K, Fig. 3a). The preferential orientation of $\{10\bar{1}0\}$ for 2-D Te gives rise to the relative intensity variation in the observed XRD patterns (Fig. 3a and Fig. S6), which indicates the morphological and structural differences for samples grown using different PVPs. This difference can also be seen in the optical images (Fig. 3a, Supplementary Figs. S1–3), which show that 2-D Te nanostructures' productivities decrease with an increase in 1-D nanowires and nanorods, with small or large molecular weight PVPs used.

The facet-specific binding of PVP onto 2-D Te during the growth is further revealed by the Fourier transform infrared spectrometer (FTIR) characterization of PVP before and after the reactions (Fig. 3b). The prominent transmission peak at 1663 cm^{-1} that is observed for PVP before the reaction represents the carbonyl group (C=O bonding) stretching vibration in the pristine PVP [54]. The FTIR spectra for the as-synthesized 2-D Te samples capped with PVP shows a shifted peak to 1643 cm^{-1} (Fig. 3b). This decrease in the wave number for the C=O stretching is thought to be attributed to the bond weakening due to the partial donation of the lone pair electrons from the oxygen atoms in PVP to the Te atoms [55], which has also been observed in the synthesis of other nanocrystals [54]. Meanwhile, no apparent shifts can be seen for the C-N vibration and H-C-H bend peaks after the reaction (Supplementary Fig. S7) due to the stable, non-ionic property of PVP in the deionized water [54]. Our first-principle calculations based on the density functional theory (DFT) (Supplementary Fig. S8) show a stretching for C=O bond in the PVP monomer from the initial 1.23–1.24 Å after it binds to the Te atoms (Fig. 3c, Supplementary Fig. S8), consistent with our FTIR results.

The facet-specific binding energies of capping agents have a profound impact on shape evolution during nanocrystal growth [56]. We further carry out DFT calculations (Supplementary Fig. S8) to identify the facet-specific binding energies of PVP on 2-D Te (Fig. 3d). In our calculations, we break the PVP monomer into 2-pyrrolidone and ethane [57] and calculate the interaction of each part with Te separately to gauge the total interaction [57]. Our results show that the binding energies of PVP monomer to Te $\{10\bar{1}0\}$, $\{\bar{1}2\bar{1}0\}$, and $\{0001\}$ are 0.40 eV, 0.32 eV, and 0.16 eV, respectively (Fig. 3d). These facet-specific binding energies of PVP suggest strong and preferential chemisorption between the PVP and the Te $\{10\bar{1}0\}$ facets that block the access of Te atoms to the $(10\bar{1}0)$ planes of the formed 2-D Te crystals. Also, the weaker PVP passivation on the side $\{\bar{1}2\bar{1}0\}$ and $\{0001\}$ facets facilitate the accommodation of Te atoms from the solution phase and hence the more rapid growth along these two directions. Consequently, the enhanced growth along the $< 1\bar{2}10 >$ and $< 0001 >$ directions lead to the formation of 2-D Te.

Based on our experimental and computational results for the interactions between PVP monomers and Te surfaces, as well as the statistical analyses of the synthesis outcomes, the effect of the PVP molecular weight on the formation of 2-D Te crystals could be understood as follows. The PVP molecule contains a strong hydrophilic component (the pyrrolidine moiety) and a significant hydrophobic group (the alkyl group) [54]. The repulsive force between the PVP molecule arises from the alkyl group [54]. Long chain PVPs contain more alkyl group, which result in stronger repulsive forces. During the nucleation and initial growth, the 2-D Te nucleus is typically smaller than the chain lengths of PVP with large molecular weights (e.g., 2 μm chain length for PVP-1300K, Supplementary Table 1). This, together with the repulsion between the adjacent PVP molecules [58] (Fig. 3e) could lead to a partially passivated $(10\bar{1}0)$ surface in the 2-D Te crystals [59]. Therefore, the Te atoms in the solution phase could readily diffuse to the exposed $(10\bar{1}0)$ surface of the 2-D Te crystals through the gaps between adjacent PVP molecules. Such confined PVP capping on the $(10\bar{1}0)$ surface due to the large PVP molecular weights thus leads to the formation of thick 2-D Te flakes and Te nanorods with large diameter (Fig. 3a and Supplementary Figs. S1-3). On the other hand, PVP molecules with small molecular weights (e.g., PVP-8K) could sufficiently passivate the $(10\bar{1}0)$ surface of Te nuclei because of the less bulky size of these PVP molecules [51] (Fig. 3e). Furthermore, these short-chain PVP molecules could pose strong passivation on the $(\bar{1}2\bar{1}0)$ and (0001) facets, in addition to the $(10\bar{1}0)$ surface, of Te nuclei, and hence significantly block the diffusion of Te atoms onto all crystal facets of Te. Consequently, the intrinsic anisotropy in the Te crystal structure favors the kinetic-driven 1-D growth and leads to a large amount of thin Te nanowires in the synthesis products (Fig. 3a, Supplementary Figs. S1-3). Lastly, when PVP with intermediate molecular weights (e.g., PVP-58K) is used, a balance between the kinetic and thermodynamic growth can be achieved due to the relatively ordered facet-selective PVP capping, and the thermodynamic-driven assembly in the $< 1\bar{2}10 >$ directions together with the continued $< 0001 >$ growth can be promoted, accompanied by the limited growth along $< 10\bar{1}0 >$ directions, all of which lead to the formation of 2-D Te nanostructures [16].

Next, control experiments are carried out that adopt other capping agents widely used in the hydrothermal synthesis of nanostructures [56] to further understand the role of PVP on the formation of 2-D Te (Supplementary Fig. S10). For this purpose, poly (ethylene glycol) (PEG), pyrrole and cetyltrimethylammonium bromide (CTAB) are used while all related reaction parameters, e.g., Na_2TeO_3/PVP mass ratio and temperature, are kept the same as to the 2-D Te synthesis with PVP. PEG is chosen for its CH_2 group, and the pyrrole has a similar pyrrolidone ring with PVP [56]. CTAB has shown strong physical adsorption to the surfaces of other nanostructures [60]. For all three control groups, only 1-D nanorods with large diameters can be observed after the reactions (Supplementary Fig. S9). Moreover, when the reaction time is extended, the lengths and diameters for these nanorods are increasing, but no 2-D Te was observed (Supplementary Fig. S9). This is likely caused by these surfactants' ineffective passivation on Te as compared to PVP [61,62]. It is also interesting to note that 1-D/2-D hybrid nanostructures with protruding lateral regions have been observed after 20-h reactions in all three control groups, similar to the intermediate structures seen in the reactions with PVP [16]. However,

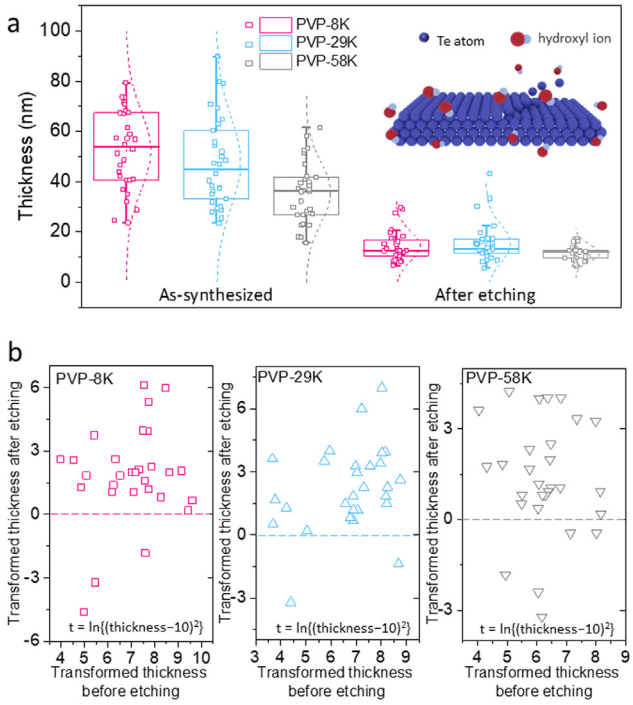

Fig. 4. Thickness and transformed thickness distribution before and after post-growth thinning process. (**a**) Thickness distribution before and after the etching process for PVP-8K, PVP-29K and PVP-58K. (**b**) Transformed thickness before and after the etching process for PVP-8K, PVP-29K and PVP-58K. The average values from 30 technical replicates are indicated, and error bars represent one standard deviation for each set of replicates.

the passivation on $(10\bar{1}0)$ facets of the formed intermediate structures are not effective enough to lead to the growth of 2-D structures. These results, together with our FTIR data, suggest that the C=O group in PVP's pyrrolidone ring, which can form the hydrogen bond with Te surface [54], are likely to be responsible for the formation of 2-D Te.

2.4. Data-driven learning of the post-growth thinning process

The 2-D Te crystal thickness can be further reduced through a solvent-assisted post-growth thinning process [16] (see Methods) (Fig. 4a, insert) involving after 6 h with acetone [16]. Such demonstrated process versatility in modulating 2-D Te thickness allows us to explore its process-dependent material properties in the 2-D limit, and uncover, for the first time, the process-structure-property relationship for solution-grown 2-D Te. We proceed to perform statistical analyses on tellurene thickness after the etching process to obtain further insights into these mechanisms.

The target thickness for the transistor application is ~10 nm, and we desire to minimize the variability of thickness. Hence, as before, our analyses are performed on the transformed thickness values given by $t = \ln((y - 10)^2)$ for observed thickness y (Fig. 4b). The experiment involves three different PVP molecular weights, with Na_2TeO_3/PVP mass ratio fixed at 1/5 and synthesis time set at 20 h. We observe in Fig. 4b that there does not exist a significant association between before- and after-etching transformed thicknesses, for any of the PVP molecular weight groups. Furthermore, this figure indicates that the after-etching transformed thicknesses are consistently centered around zero. Both of these observations suggest that the etching process has a consistent and stable effect on the 2-D Te crystal thickness that does not depend on pre-the etching thickness or molecular weight.

For each PVP molecular weight group, paired t-tests on the samples indicate statistically significant differences between before- and after-etching thicknesses at the 0.05 level (the p-value is less than 0.0001 for each PVP molecular weight group). The etching process is estimated to reduce tellurene thickness (in expectation) by (i) 23.93 nm for PVP-58K, (ii) 39.11 nm for PVP-29K, and (iii) 32.18 nm for PVP-8K. We formally evaluate the effects of PVP molecular weights on after-etching transformed thicknesses via linear regression. The fitted model is

$$\hat{t_e} = 12.14 + 2.1 \quad I_{PVP-29K} + 9.8 \quad \times 10^{-1} I_{PVP-8K}, \tag{6}$$

where $\hat{t_e}$ denotes the predicted transformed thickness after etching. The p-values for the two regression coefficients in this model are greater than the significance level of 0.05, indicating that PVP molecular weight is not a statistically significant predictor for after-etching thickness. In light of this result, we combine all of the selected PVP molecular weight groups to estimate the mean thickness after etching as 13.15 nm and the standard deviation of after-etching thickness as 5.70 nm. The 95% confidence interval for mean thickness after etching is (11.92 nm, 14.37 nm). Although the target value of 10 nm does not lie in this interval, we can still conclude from our analysis that tellurene thickness is significantly reduced in a practical sense by the etching process.

2.5. Process-engineered electrical properties of 2-D Te

Finally, we explore the process-dependent electrical performances of 2-D Te field-effect transistors (FETs). Back-gate devices are fabricated following the reported procedures [16] (see Methods). We use Pd/Au as the metal contacts since Pd has a relatively high work function which benefits the formation of Ohmic contacts in p-type transistors [16]. The typical transport and transfer curves of 2-D Te FETs are shown in Fig. 5a-b. A linear I-V relationship is observed in the transfer curves (Fig. 5a) when the drain bias is low, indicating the excellent contact properties between the metal electrodes and 2-D Te [16]. An excellent current saturation at high drain bias is also observed, with the highest drain current density of 217 mA/mm occurring for the V_{bg} = –30 V and V_{ds} = -2 V. The transfer curves show a decent on/off ratio of ~10^4. We further study the process dependence of two key metrics of the electrical performance of 2-D Te FETs, namely the field-effect mobilities and on/off ratios (Fig. 5c-d). We randomly selected 30 flakes derived from the processes using three different PVP molecules and fabricated the back-gate FETs. We then extracted the field-effect mobility from the slope of the linear region of the transfer curves [5]. Similar to other 2-D materials based transistors, 2-D Te FETs show a clear thickness-dependence for the field-effect mobility (Fig. 5c), which peaks at around 10 nm thickness and decreases with the increased thickness due to the thickness-dependent charge screening and interlayer coupling [4,16,63–65]. It should be noted that different process factors (e.g., PVP molecular weights) lead to significantly different mean values and variations for the devices' field-effect mobilities (Fig. 5c-d).

We perform formal statistical analyses on the electrical performances of 2-D Te in a similar manner as before. Specifically, we first learn the effects of PVP molecular weights on the mobility and on/off ratio of a tellurene device, and then, for each of these performance measures, we identify the PVP molecular weights that can maximize it in expectation and minimize its variance. The experiment involves three different PVP molecular weights, with PVP concentration fixed at mass ratio 1/5 and synthesis time set at 20 h. Our first statistical analysis is on mobility. Two separate linear regression models were fit to study the effects of PVP molecular weight on its expectation and variance. The fitted weighted linear regression model for the expectation is

$$\hat{m} = 495.5 - 51.72 \quad I_{PVP-29K} - 26.36 \quad I_{PVP-8K}, \tag{7}$$

where $\hat{m}$ denotes the predicted mobility and I_{PVP-i} is the indicator variable for PVP molecular weight i. Again, to prevent over-parameterization in the model, the indicator $I_{PVP-58K}$ is omitted, and its predicted mobility is equal to the intercept estimate of 495.5. The model fit for the standard deviation is

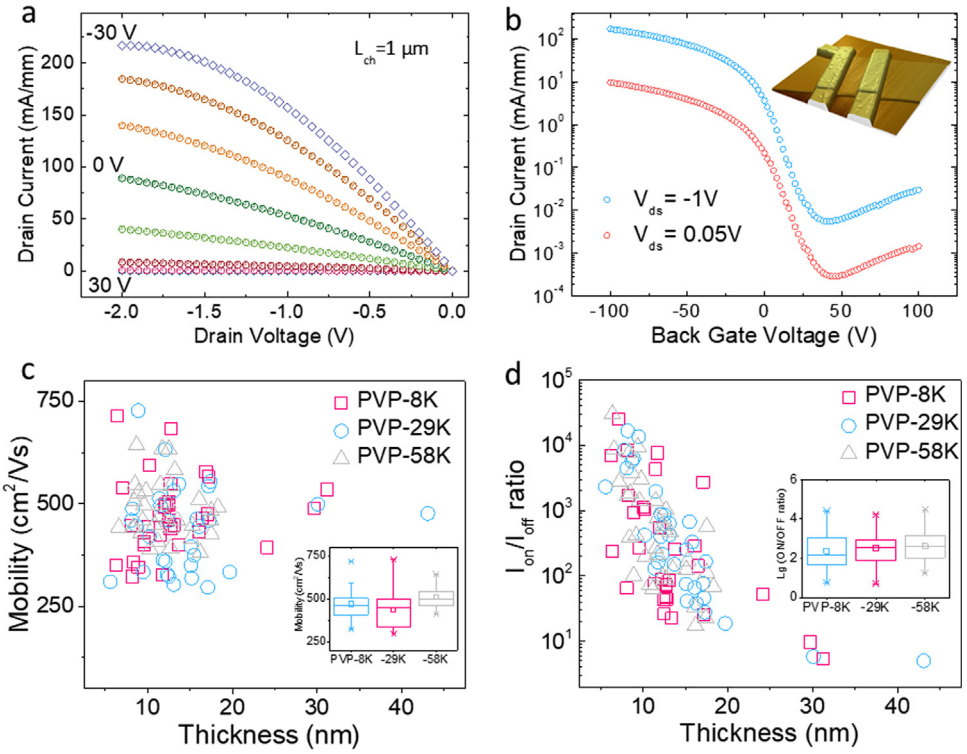

Fig. 5. Process-engineered performance of 2-D tellurene field-effect-transistors. (**a and b**) Output and transfer curves of 2-D tellurene transistor with a film thickness of 15.8 nm. The inset is the AFM image of the FET device. (**c and d**) The statistical distributions mobility and on/off ratio of 2-D tellurene FET obtained with different PVP chain lengths. The average values from 30 technical replicates are indicated, and error bars represent one standard deviation for each set of replicates.

$$\hat{\sigma}_m = 52.90 + \quad 31.10 \quad I_{PVP-29K} + 18.47 \quad I_{PVP-8K} \tag{8}$$

where $\hat{\sigma}_m$ is the estimated standard deviation of mobility. Similarly to Eq. (7), the predicted standard deviation for PVP-58K is equal to the intercept estimate of 52.90. In both of the models in Eqs. (7) and (8), the only statistically significant difference between the PVP molecular weights at the 0.05 significance is that between PVP-58K and PVP-29K. These results indicate that PVP-58K potentially maximizes mobility while reducing its variance.

Our final statistical analysis is on the on/off ratio. We transform each device's on/off ratio using the base 10 logarithm. The weighted linear regression model fit for the expectation is

$$\log_{10}(r) = 2.5 + 6.9 \quad \times 10^{-2} I_{PVP-29K} - 1.3 \times 10^{-1} I_{PVP-8K}, \tag{9}$$

where $\log_{10}(r)$ is the prediction for the base 10 logarithm of on/off ratio. The *p*-values for the regression coefficients are not significant at the 0.05 level, and so we can conclude that PVP molecular weight does not have a statistically significant effect on the expectation of the transformed on/off ratio. The model fit for the standard deviation is

$$\hat{\sigma}_{\log_{10}} = 5.3 \quad \times 10^{-1} + \quad 1.3 \quad \times 10^{-1} I_{PVP-29K} \quad + \quad 2.8 \quad \times 10^{-1} I_{PVP-8K}, \tag{10}$$

where $\hat{\sigma}_{\log_{10}(r)}$ is the estimated standard deviation of the base 10 logarithm of the on/off ratio. The regression coefficient for PVP-29K in Eq. (10) is the only statistically significant model parameter at the 0.05 level. Thus, we conclude that PVP-58K can potentially minimize the variability of on/off ratio in tellurene devices. These two statistical analyses correspond to the observation from Fig. 5c-d that the optimum mobility and on/off ratio values occur for devices that possess thicknesses of approximately 10 nm.

3. Conclusion

We performed a systematic study and data-driven learning of the effects of fundamental process factors on production outcomes for solution-grown tellurene. Our study involved a holistic and synergistic integration of both experimental explorations and statistical analyses. In particular, we identified the roles of PVP in the modulation of production yield, dimensions, and physical properties of the as-synthesized tellurene materials. We further demonstrated a closed-loop cycle, where the fundamental synthesis knowledge was uncovered through the learning of a limited amount of initial experiments, and valuable insights were generated for guiding the design and optimization of the nanomanufacturing process for tellurene. Lastly, we demonstrated the application of such fundamental knowledge to develop tellurene transistors with optimized performance. Compared to the reported performance merits for tellurene transistors [16], the results shown here in this work present similar mean values for the field-effect mobilities and on/off ratios, but with improved control over the standard deviation for both figure-of-merits. Our research is expected to help develop a comprehensive understanding of the fundamental manufacturing science for producing a new class of 2-D materials through a low-cost, scalable liquid solution method. This capability will establish a solid foundation for facilitating further investigations of tellurene's intriguing properties. Ultimately, our work will enable the modeling, design, manufacture, integration, and optimization of tellurene in advanced electronics, quantum devices, sensors, and the related technological implementation to be performed in more effective, affordable, and sustainable manners [66–69].

4. Materials and methods

4.1. Materials

PVP-8K, PVP-29K, PVP-58K, PVP-360K, PVP-1300K, hydrazine hydrate (85%, w/w), acetone, aqueous ammonia solution (25–28%, w/w), N, N-dimethylformamide (DMF), $CHCl_3$ were purchased from Sigma Aldrich. Na_2TeO_3 (97%) was purchased from Alfa Aesar. All chemical reagents were used without further purification. Double-distilled deionized water (18.2 Megaohms) was used for the synthesis.

4.2. Synthesis of 2-D Te crystals and post-thinning process

In the typical synthesis, Na_2TeO_3 and PVP were put into double distilled water at room temperature under magnetic stirring to form a

homogeneous solution. The resulting solution was poured into a Teflon-lined steel autoclave, which was then filled with aqueous ammonia solution and hydrazine hydrate. The autoclave was sealed and maintained at the reaction temperature for a designed time. Then the autoclave was cooled to room temperature naturally. The resulting silver-gray products were precipitated by centrifuge at 5000 rpm for 5 min and washed with distilled water (to remove any ions remaining in the final product). For the Post-thinning process, the fresh 2-D Te solution was dispersed into acetone. The solution was kept at room temperature for six hours. Finally, the thinned tellurene samples were precipitated by centrifugation.

4.3. Langmuir-Blodgett (LB) transfer of 2-D Te

The hydrophilic 2-D Te nanoflake monolayers can be transferred to various substrates by the Langmuir-Blodgett (LB) technique. The washed 2-D Te were mixed with N, N-dimethylformamide (DMF) and $CHCl_3$. Then the above solution was dropped into the deionized water. After 30 min, the monolayer 2-D Te can be transferred to any substrates.

4.4. Determination of the 2-D Te productivity

1 ml as-synthesized 2-D solution was mixed with 2 ml acetone and centrifuged at 5000 rpm for 5 min. After being washed twice, the 2-D Te flakes were dispersed into 3 ml of deionized water. After that, 100 ul of the above solution was dropped on the $1 \times 1\ cm^2$ SiO_2/Si substrate. We used an optical microscope to record several images that randomly covered the $5 \times 5\ mm^2$ area. Finally, we analyzed the areas covered by 2-D tellurene using ImageJ, a public domain, Java-based image processing program developed at the National Institutes of Health. In our case, we define the productivity as the ratio of the 2-D Te area in the entire image.

4.5. Data-driven methods for learning the underlying mechanisms of 2-D Te synthesis

4.5.1. Linear regression model

Regression analysis is a widely used statistical methodology for modeling the relationships between a response variable y and a vector of explanatory variables X [52]. The regression model has the form

$$Y = \boldsymbol{X}\beta + \epsilon,$$

where Y is the $n \times 1$ vector of responses for all units of analysis, $\boldsymbol{X}$ is a $n \times p$ matrix of their explanatory variables, β is a $p \times 1$ vector of unknown coefficients for the explanatory variables that is to be estimated, and ϵ is a $n \times 1$ vector of random error terms that are independent and identically distributed as $N(0, \sigma^2)$ random variables. A standard estimator of β is the least squares estimator $\hat{\beta} = (\boldsymbol{X}^T\boldsymbol{X})^{-1}\boldsymbol{X}^T Y$, which is obtained by minimizing the squared error $(Y - \boldsymbol{X}\beta)^T(Y - \boldsymbol{X}\beta)$ with respect to β. Given $\hat{\beta}$, the fitted linear model is obtained as

$$\hat{y} = X^T\hat{\beta}.$$

A standard estimator for σ^2 is based on the residuals sum of squares for the fitted linear model, and is defined as $\hat{\sigma}^2 = (Y - \boldsymbol{X}\hat{\beta})^T(Y - \boldsymbol{X}\hat{\beta})/(n - p)$. Using regression analysis, we can learn the relationships between process factors and 2-D Te production outcomes, and identify the process factors' levels that can optimize them.

4.5.2. The weighted linear regression model

It is important to note that the previously described linear regression model assumes a constant (and unknown) variance σ^2 for all observations. An alternative model when this assumption is violated is the weighted linear regression model. This is fit to the data by using the following iterative weighted least squares procedure [47].

1. Fit a linear regression for the response variable, $\hat{y} = X^T\hat{\beta}$, and analyze the vector of residuals $e = Y - \hat{Y}$ to check the model assumptions.
2. In the non-constant variance case, obtain $\hat{\sigma}_Y = \boldsymbol{X}\hat{\gamma}$ by regressing the absolute values of the residuals on the explanatory variables.
3. Use the model in Step 2 to obtain estimates for the weights as $w=1/(\hat{\sigma}_z)^2$.
4. Estimate the regression coefficients as $\hat{\beta} = (\boldsymbol{X}^T\boldsymbol{W}\boldsymbol{X})^{-1}\boldsymbol{X}^T\boldsymbol{W}Y$, where $\boldsymbol{W}$ is the diagonal matrix whose diagonal entries consist of the weights w.
5. If the coefficients obtained in Step 4 differ substantially from those in Step 1, iterate Steps 2–4 again, using the residuals from the model in Step 4 for the new iteration of Step 2.

Once the estimates have been calculated and the final fitted model has been diagnosed, we then find the process factors' settings that optimize the outcomes of interest. This step is further described below.

4.6. Optimization of an outcome's expectation and variance via regression models

Consider our goals of identifying the process factors' settings that yield a specified thickness in expectation, maximize width and productivity in expectation, and minimize the variability for all of these outcomes. To address the objectives for width and productivity, we followed the sequential approach [48], outlined below.

1. Identify the factors that affect the expectation of the process outcome.
2. Learn from the data how to set the levels of factors identified in Step 1 to achieve the desired expectation.
3. Identify the factors that affect the variance of the outcome but not its expectation.
4. Learn from the data how to set the levels of the factors identified in Step 3 to minimize variance.

As demonstrated in our analyses, it is not always possible to identify factors that affect the variance but not the expectation of the outcome. In such a case, if a target value for an outcome can be identified, then an alternative to the sequential approach above is to minimize a quadratic loss function for the outcome [48]. To illustrate, consider thickness. As the desired thickness is 10 nm, we can define the loss of the deviation of the thickness y from the target by means of the quadratic loss function $L(y, 10) = (y-10)^2$. Its expectation $E\{L(y, 10)\}$ can be expressed as

$$E\{L(y, 10)\} = \mathrm{Var}(y) + \{E(y)-10\}^2,$$

where and $E(y)$ represent the variance and expectation of thickness, respectively. By inspection of the equation above, we have that the loss can be minimized in expectation by selecting factor levels that minimize the thickness variance and move its expectation close to the target. Thus, by minimizing the quadratic loss, we optimize the combination of the expectation and variance of thickness. In practice, the fact that the quadratic loss is always positive motivates performing statistical analyses on its logarithmic transformation.

4.7. Validation experiments to confirm the optimized thickness

4.7.1. Estimated optimum mass ratio

To identify the mass ratio levels that optimize transformed thickness, we consider two possible approaches. First, we set the optimum target transformed thickness at 5.89 based on our model's predictions, and test whether the mean transformed thickness at mass ratio 0.26667, $\mu_{0.26667}$, is significantly different from the target value of 5.89. Here, we are testing whether the mean transformed thickness at mass ratio 0.26667 is significantly different from the prediction given by our model described in Eq. (3). Second, we compare mean thickness and

mean transformed thickness at two different mass ratios, 0.26667 and 0.20. Mass ratio 0.20 is of interest as it resulted in the apparent best outcome in our initial experiments.

4.7.1.1. One sample t-test for mean transformed thickness at mass ratio 0.26667. Let the target transformed thickness be 5.89. We will test whether the mean transformed thickness at mass ratio 0.26667 is significantly different from the target transformed thickness of 5.89. Our null and alternative hypotheses are

$H_0 : \mu_{0.26667} = 5.89$

$H_1 : \mu_{0.26667} \neq 5.89$

The *t*-test statistic value is -0.46, and the p-value is 0.6567. Thus, at the 5% significance level, we can conclude that there is no evidence to suggest that mean transformed thickness at mass ratio 0.26667 is different from our model's prediction, and the target value of 5.89.

4.7.1.2. Two samples t-tests. We next compare thickness and transformed thickness at two mass ratios, the optimum mass ratio 0.26667 and mass ratio of 0.20. First, we test for thickness under the hypotheses

$H_0 : \mu_{0.26667} = \mu_{0.20}$

$H_1 : \mu_{0.26667} \neq \mu_{0.20}$

The *t*-test statistic value is -0.77, and the p-value is 0.4543. Thus, at the 5% significance level, we can conclude that there is no evidence to suggest that mean thickness is different at the different mass ratios.

Finally, we compare transformed thickness for the two mass ratios under the same type of null and alternative hypotheses as above. The *t*-test statistic is -0.68, and the p-value is 0.5068. Thus, again, at the 5% significance level, we can conclude that there is no evidence to suggest a difference between the mean transformed thickness for the two mass ratios. From all of these results, we can conclude that, in a practical sense, the mass ratio of 0.20 can be considered an optimum value.

4.8. Density functional theory (DFT) calculation

Geometric optimizations and total energy calculations were performed employing density functional theory and projector augmented wave (WAV) pseudopotentials. Generalized gradient approximation (GGA) in the scheme of Perdew-Burke-Ernzerhof (PBE) is used to describe the exchange-correlation. We used 300 eV for the plane-wave cutoff, 4 × 4 × 1 Monkhorst-Pack sampling, and the system was fully relaxed until the final force was less than 0.05 eV/Å on each atom. In order to evaluate the interaction of PVP with Te surfaces, a breakdown method was used, and PVP was replaced by 2-pyrrolidone. Te surfaces were modeled by period slabs using supercell with six Te layers and vacuum layer with a thickness of 15 Å. Tkatchenko–Scheffler PBE + vdW schemes were used to take the van der Waals attraction into consideration.

4.9. FET device fabrication and transport measurement

After the 2-D Te transferring the tellurene flakes onto the substrate, source and drain regions were patterned by electron-beam lithography (EBL). We chose 50/50 nm Pd/Au for the contact metal. The transport measurements were performed using a Keithley 4200A semiconductor characterization system. By plugging numbers into the formula:

$\mu_{FE} = g_m L / W C_{ox} V_{ds}$

where g_m, L, W and, C_{ox} are transconductance, channel length, channel width and gate oxide capacitance, we can derive the field-effect mobilities for the 2-D Te transistors.

4.10. Instrumentation

The size of the 2-D Te crystals was identified by optical microscopy (Olympus BX-60). The thickness was determined by AFM (Keysight 5500). XRD analyses were carried by Bruker D8 with Cu Kα radiation. The structure of the PVP was analyzed by Fourier transform infrared spectrometer (FT-IR, Thermo Nicolet Nexus, using KBr beam splitter).

Acknowledgements

W. Z. W. acknowledges the College of Engineering and School of Industrial Engineering at Purdue University for the startup support. W. Z. W. was partially sponsored by the National Science Foundation under Grant CMMI-1762698. W. Z. W. and P. D. Y. were partially supported by the Army Research Office under Grant nos. W911NF-15-1-0574 and W911NF-17-1-0573. P. D. Y. was supported by the NSF/AFOSR 2DARE Program and SRC.

Author contributions

W. Z. W. conceived and supervised the project. W. Z. W., A. S., Y. X. W., and R. D. S. B. F. designed the experiments. Y. X. W. and R. X. W. synthesized the material. Y. X. W. and G. Q. fabricated the devices. G. Q. performed the electrical characterization under the supervision of P. D. Y. G. D. L. carried out the first-principles calculations under the supervision of W. Z. W., and Y. Q. W. Z. W., A. S., Y. X. W., and R. D. S. B. F. analyzed the data. W. Z. W., A. S., Y. X. W., and R. D. S. B. F. wrote the manuscript. All authors have discussed the results and commented on the paper.

Competing financial interests

The authors declare no competing financial interests.

Online content

Methods, along with any additional Extended Data display items are available in the online version of the paper. References unique to these sections appear only in the online paper.

Appendix A. Supplementary material

Supplementary data associated with this article can be found in the online version at doi:10.1016/j.nanoen.2018.12.065.

References

[1] A.D. Franklin, Science 349 (2015) 704.
[2] S.B. Desai, S.R. Madhvapathy, A.B. Sachid, J.P. Llinas, Q. Wang, G.H. Ahn, G. Pitner, M.J. Kim, J. Bokor, C. Hu, H.S.P. Wong, A. Javey, Science 354 (2016) 99.
[3] H. Wang, L. Yu, Y.-H. Lee, Y. Shi, A. Hsu, M.L. Chin, L.-J. Li, M. Dubey, J. Kong, T. Palacios, Nano Lett. 12 (2012) 4674–4680.
[4] L. Li, Y. Yu, G.J. Ye, Q. Ge, X. Ou, H. Wu, D. Feng, X.H. Chen, Y. Zhang, Nat. Nanotechnol. 9 (2014) 372–377.
[5] H. Liu, A.T. Neal, Z. Zhu, Z. Luo, X. Xu, D. Tománek, P.D. Ye, ACS Nano 8 (2014) 4033–4041.
[6] G. Iannaccone, F. Bonaccorso, L. Colombo, G. Fiori, Nat. Nanotechnol. 13 (2018) 183–191.
[7] C.R. Dean, A.F. Young, I. Meric, C. Lee, L. Wang, S. Sorgenfrei, K. Watanabe, T. Taniguchi, P. Kim, K.L. Shepard, J. Hone, Nat. Nanotechnol. 5 (2010) 722–726.
[8] W. Cao, J. Kang, D. Sarkar, W. Liu, K. Banerjee, IEEE Trans. Electron Devices 62 (2015) 3459–3469.
[9] B. Radisavljevic, A. Radenovic, J. Brivio, V. Giacometti, A. Kis, Nat. Nanotechnol. 6 (2011) 147–150.
[10] L. Tao, E. Cinquanta, D. Chiappe, C. Grazianetti, M. Fanciulli, M. Dubey, A. Molle, D. Akinwande, Nat. Nanotechnol. 10 (2015) 227–231.
[11] H. Fang, S. Chuang, T.C. Chang, K. Takei, T. Takahashi, A. Javey, Nano Lett. 12 (2012) 3788–3792.
[12] Y. Hao, M.S. Bharathi, L. Wang, Y. Liu, H. Chen, S. Nie, X. Wang, H. Chou, C. Tan, B. Fallahazad, H. Ramanarayan, C.W. Magnuson, E. Tutuc, B.I. Yakobson, K.F. McCarty, Y.-W. Zhang, P. Kim, J. Hone, L. Colombo, R.S. Ruoff, Science 342 (2013) 720.
[13] S. Najmaei, Z. Liu, W. Zhou, X. Zou, G. Shi, S. Lei, B.I. Yakobson, J.-C. Idrobo, P.M. Ajayan, J. Lou, Nat. Mater. 12 (2013) 754–759.
[14] A.J. Mannix, X.-F. Zhou, B. Kiraly, J.D. Wood, D. Alducin, B.D. Myers, X. Liu, B.L. Fisher, U. Santiago, J.R. Guest, M.J. Yacaman, A. Ponce, A.R. Oganov, M.C. Hersam, N.P. Guisinger, Science 350 (2015) 1513.
[15] F.-F. Zhu, W.-J. Chen, Y. Xu, C.-L. Gao, D.-D. Guan, C.-H. Liu, D. Qian, S.-C. Zhang,

J.-F. Jia, Nat. Mater. 14 (2015) 1020–1025.
[16] Y. Wang, G. Qiu, R. Wang, S. Huang, Q. Wang, Y. Liu, Y. Du, W.A. Goddard, M.J. Kim, X. Xu, P.D. Ye, W. Wu, Nat. Electron. 1 (2018) 228–236.
[17] M.M. Shulaker, G. Hills, R.S. Park, R.T. Howe, K. Saraswat, H.S.P. Wong, S. Mitra, Nature 547 (2017) 74.
[18] F.A. McGuire, Y.-C. Lin, K. Price, G.B. Rayner, S. Khandelwal, S. Salahuddin, A.D. Franklin, Nano Lett. 17 (2017) 4801–4806.
[19] M. Si, C.-J. Su, C. Jiang, N.J. Conrad, H. Zhou, K.D. Maize, G. Qiu, C.-T. Wu, A. Shakouri, M.A. Alam, P.D. Ye, Nat. Nanotechnol. 13 (2018) 24–28.
[20] G. Fiori, F. Bonaccorso, G. Iannaccone, T. Palacios, D. Neumaier, A. Seabaugh, S.K. Banerjee, L. Colombo, Nat. Nanotechnol. 9 (2014) 768–779.
[21] D.A. Bandurin, A.V. Tyurnina, G.L. Yu, A. Mishchenko, V. Zólyomi, S.V. Morozov, R.K. Kumar, R.V. Gorbachev, Z.R. Kudrynskyi, S. Pezzini, Z.D. Kovalyuk, U. Zeitler, K.S. Novoselov, A. Patanè, L. Eaves, I.V. Grigorieva, V.I. Fal'ko, A.K. Geim, Y. Cao, Nat. Nanotechnol. 12 (2016) 223.
[22] D. Sarkar, X. Xie, W. Liu, W. Cao, J. Kang, Y. Gong, S. Kraemer, P.M. Ajayan, K. Banerjee, Nature 526 (2015) 91.
[23] S. Salahuddin, S. Datta, Nano Lett. 8 (2008) 405–410.
[24] Y. Liu, J. Guo, E. Zhu, L. Liao, S.-J. Lee, M. Ding, I. Shakir, V. Gambin, Y. Huang, X. Duan, Nature 557 (2018) 696–700.
[25] Z. Zhang, P. Chen, X. Duan, K. Zang, J. Luo, X. Duan, Science (2017).
[26] M.Y. Li, Y.M. Shi, C.C. Cheng, L.S. Lu, Y.C. Lin, H.L. Tang, M.L. Tsai, C.W. Chu, K.H. Wei, J.H. He, W.H. Chang, K. Suenaga, L.J. Li, Science 349 (2015) 524–528.
[27] L. Wang, I. Meric, P.Y. Huang, Q. Gao, Y. Gao, H. Tran, T. Taniguchi, K. Watanabe, L.M. Campos, D.A. Muller, J. Guo, P. Kim, J. Hone, K.L. Shepard, C.R. Dean, Science 342 (2013) 614–617.
[28] F. Xia, V. Perebeinos, Y.-M. Lin, Y. Wu, P. Avouris, Nat. Nanotechnol. 6 (2011) 179.
[29] F. Léonard, A.A. Talin, Nat. Nanotechnol. 6 (2011) 773.
[30] M. Chhowalla, D. Jena, H. Zhang, Nat. Rev. Mater. 1 (2016) 16052.
[31] K.S. Novoselov, A.K. Geim, S.V. Morozov, D. Jiang, Y. Zhang, S.V. Dubonos, I.V. Grigorieva, A.A. Firsov, Science 306 (2004) 666–669.
[32] P.K. Sahoo, S. Memaran, Y. Xin, L. Balicas, H.R. Gutiérrez, Nature 553 (2018) 63.
[33] J. Zhou, J. Lin, X. Huang, Y. Zhou, Y. Chen, J. Xia, H. Wang, Y. Xie, H. Yu, J. Lei, D. Wu, F. Liu, Q. Fu, Q. Zeng, C.-H. Hsu, C. Yang, L. Lu, T. Yu, Z. Shen, H. Lin, B.I. Yakobson, Q. Liu, K. Suenaga, G. Liu, Z. Liu, Nature 556 (2018) 355–359.
[34] F. Teng, K. Hu, W. Ouyang, X. Fang, Adv. Mater. 30 (2018) 1706262.
[35] Y. Yoon, K. Ganapathi, S. Salahuddin, Nano Lett. 11 (2011) 3768–3773.
[36] H. Liu, A.T. Neal, P.D. Ye, ACS Nano 6 (2012) 8563–8569.
[37] S. Das, H.-Y. Chen, A.V. Penumatcha, J. Appenzeller, Nano Lett. 13 (2013) 100–105.
[38] X. Li, W. Cai, J. An, S. Kim, J. Nah, D. Yang, R. Piner, A. Velamakanni, I. Jung, E. Tutuc, S.K. Banerjee, L. Colombo, R.S. Ruoff, Science 324 (2009) 1312–1314.
[39] J.N. Coleman, M. Lotya, A. O'Neill, S.D. Bergin, P.J. King, U. Khan, K. Young, A. Gaucher, S. De, R.J. Smith, I.V. Shvets, S.K. Arora, G. Stanton, H.-Y. Kim, K. Lee, G.T. Kim, G.S. Duesberg, T. Hallam, J.J. Boland, J.J. Wang, J.F. Donegan, J.C. Grunlan, G. Moriarty, A. Shmeliov, R.J. Nicholls, J.M. Perkins, E.M. Grieveson, K. Theuwissen, D.W. McComb, P.D. Nellist, V. Nicolosi, Science 331 (2011) 568–571.
[40] F. Bonaccorso, A. Lombardo, T. Hasan, Z. Sun, L. Colombo, A.C. Ferrari, Mater. Today 15 (2012) 564–589.
[41] A. Amey, B. Elisabeth, K. Aravind, Y. Sadegh, R. Rahul, G. Nicholas, K. Hiroyuki, V. Vikas, R. Ajit, S. Fuyuki, R. Emilie, K.K. Rajiv, N. Aiichiro, T. Chandra Sekhar, V. Priya, K. Vidya, M.A. Pulickel, 2D Mater. 6 (2019) 015013.
[42] Y. Liu, W. Wu, W.A. Goddard, J. Am. Chem. Soc. 140 (2018) 550–553.
[43] J. Qiao, Y. Pan, F. Yang, C. Wang, Y. Chai, W. Ji, Sci. Bull. 63 (2018) 159–168.
[44] Z. Zhu, X. Cai, S. Yi, J. Chen, Y. Dai, C. Niu, Z. Guo, M. Xie, F. Liu, J.-H. Cho, Y. Jia, Z. Zhang, Phys. Rev. Lett. 119 (2017) 106101.
[45] X. Huang, J. Guan, Z. Lin, B. Liu, S. Xing, W. Wang, J. Guo, Nano Lett. 17 (2017) 4619–4623.
[46] Y. Du, G. Qiu, Y. Wang, M. Si, X. Xu, W. Wu, P.D. Ye, Nano Lett. 17 (2017) 3965–3973.
[47] S.J. Gao, Y.X. Wang, R.X. Wang, W.Z. Wu, Semicond. Sci. Technol. 32 (2017) 104004.
[48] M.-L. Tsai, M.-Y. Li, J.R.D. Retamal, K.-T. Lam, Y.-C. Lin, K. Suenaga, L.-J. Chen, G. Liang, L.-J. Li, J.-H. He, Adv. Mater. 29 (2017) 1701168.
[49] C.-P. Lee, K.-Y. Lai, C.-A. Lin, C.-T. Li, K.-C. Ho, C.-I. Wu, S.-P. Lau, J.-H. He, Nano Energy 36 (2017) 260–267.
[50] W. Zhang, C.-P. Chuu, J.-K. Huang, C.-H. Chen, M.-L. Tsai, Y.-H. Chang, C.-T. Liang, Y.-Z. Chen, Y.-L. Chueh, J.-H. He, M.-Y. Chou, L.-J. Li, Sci. Rep. 4 (2014) 3826.
[51] Z. Xiping, Z. Bingpu, G. Yibo, W. Cong, L. Shunbo, Y. Chau Yeung, W. WeiJia, Nanotechnology 25 (2014) 495601.
[52] N. Kutner, Li Neter, Applied Linear Statistical Models, McGraw-Hill, New York, NY, 2005.
[53] C.F.Ja.H. Wu, Experiments: Planning, Analysis, and Optimization, Wily, 2009.
[54] K.M. Koczkur, S. Mourdikoudis, L. Polavarapu, S.E. Skrabalak, Dalton Trans. 44 (2015) 17883–17905.
[55] Y. Gao, P. Jiang, D.F. Liu, H.J. Yuan, X.Q. Yan, Z.P. Zhou, J.X. Wang, L. Song, L.F. Liu, W.Y. Zhou, G. Wang, C.Y. Wang, S.S. Xie, J.M. Zhang, D.Y. Shen, J. Phys. Chem. B 108 (2004) 12877–12881.
[56] W. Shi, S. Song, H. Zhang, Chem. Soc. Rev. 42 (2013) 5714–5743.
[57] W.A. Al-Saidi, H. Feng, K.A. Fichthorn, Nano Lett. 12 (2012) 997–1001.
[58] M. Tsuji, Y. Nishizawa, K. Matsumoto, M. Kubokawa, N. Miyamae, T. Tsuji, Mater. Lett. 60 (2006) 834–838.
[59] J.-J. Zhu, C.-X. Kan, J.-G. Wan, M. Han, G.-H. Wang, J. Nanomater. 2011 (2011) 1–7.
[60] B.D. Busbee, S.O. Obare, C.J. Murphy, Adv. Mater. 15 (2003) 414–416.
[61] J.-W. Liu, J.-H. Zhu, C.-L. Zhang, H.-W. Liang, S.-H. Yu, J. Am. Chem. Soc. 132 (2010) 8945–8952.
[62] J.-W. Liu, J. Xu, H.-W. Liang, K. Wang, S.-H. Yu, Angew. Chem. Int. Ed. 51 (2012) 7420–7425.
[63] R. Resta, Phys. Rev. B 16 (1977) 2717–2722.
[64] Y. Sui, J. Appenzeller, Nano Lett. 9 (2009) 2973–2977.
[65] S. Das, J. Appenzeller, Phys. Status Solidi RRL 7 (2013) 268–273.
[66] W.Z. Wu, G. Qiu, Y.X. Wang, R.X. Wang, P.D. Ye, Chem. Soc. Rev. 47 (2018) 7203–7212.
[67] G. Qiu, M. Si, Y. X. Wang, X. Lyu, W. Z. Wu, P. D. Ye, 2018 76th Device Research Conference (DRC), Santa Barbara, CA, 2018, pp. 1–2. doi: ⟨http://doi.org/10.1109/DRC.2018.8442253⟩.
[68] Y.X. Wang, R.X. Wang, S.H. Wan, Q.X. Wang, M.J. Kim, D. Ding, W.Z. Wu, Nano Futures (2018), https://doi.org/10.1088/2399-1984/aaf76f.
[69] G. Qiu, Y.X. Wang, Y.F. Nie, Y.P. Zheng, K. Cho, W.Z. Wu, P.D. Ye, Nano Lett. 18 (2018) 5760–5767.

Yixiu Wang received his MS degree in Material Science and Engineering from the University of Science and Technology of China (USTC) under the supervision of Prof. Shu-Hong Yu in 2014. He is currently pursuing his PhD in the Department of Industrial Engineering under the supervision of Prof. Wenzhuo Wu. His main research activity focuses on low dimensional material synthesis and novel 2D atomic crystals targeting nanoelectronics and energy conversion devices together with the exploration of fundamental phenomena in nanoscale systems.

Raquel de Souza Borges Ferreira is currently pursuing her Ph.D.'s degree in Statistics under the supervision of Prof. Arman Sabbaghi at Purdue University. Her dissertation is focused on interpretable machine learning for additive manufacturing systems.

Ruoxing Wang received her BS degree in Chemistry in 2015 from University of Science and Technology of China (USTC). She is currently a PhD student in Industrial Engineering at Purdue University under the supervision of Prof. Wenzhuo Wu. Her research interests mainly focus on nanomanufacturing including the design of functional nanomaterials and fabrication of nanodevices for various applications.

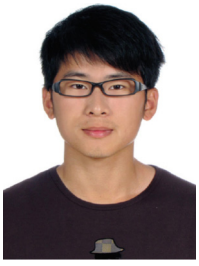

Gang Qiu received his BS degree in microelectronics from Peking University, Beijing, China in 2014. He is currently working towards his PhD degree at School of Electrical and Computer Engineering in Purdue University, West Lafayette, Indiana, USA, under the supervision of Prof. Peide. D. Ye. His current research interests focus on novel low dimensional material synthesis and characterization, potential electronic device applications and low-temperature magneto-transport.

Gaoda Li received his B.S. in Physics from Lanzhou University, China in 2013. Now he is a Ph.D. student in School of Physical Science and Technology of Lanzhou University at Institute of Nanoscience and Nanotechnology. His research mainly focuses on the physical properties influenced by surface chemisorption.

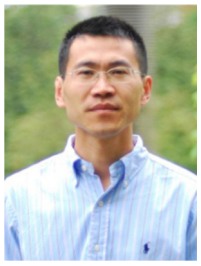

Yong Qin received his B.S. (1999) in Material Physics and Ph.D. (2004) in Material Physics and Chemistry from Lanzhou University. From 2007 to 2009, he worked as a visiting scholar and Postdoc in Professor Zhong Lin Wang's group at Georgia Institute of Technology. Currently, he is a professor at the Institute of Nanoscience and Nanotechnology, Lanzhou University. His research interests include nanoenergy technology, functional nanodevice and self-powered nanosystem.

Dr Peide Ye is Richard J. and Mary Jo Schwartz Professor of Electrical and Computer Engineering at Purdue University, USA. He received his PhD from the Max Planck-Institute of Solid State Research, Stuttgart, Germany, in 1996. Before joining the Purdue faculty in 2005, he worked for NTT Basic Research Laboratory, NHMFL/Princeton University, and Bell Labs/Lucent Technologies/ Agere Systems. His current research work is focused on atomic layer deposition technology and its device integration on novel channel materials including III–V, Ge, 2D materials and complex oxides. He has authored and co-authored more than 200 peer reviewed articles and 350 conference presentations including many invited, keynote and plenary talks. He has also served as a chairman and a program committee member on top international conferences and symposia. He is a Fellow of IEEE and the APS (American Physical Society).

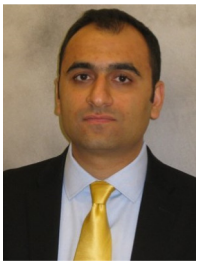

Arman Sabbaghi is an Assistant Professor and Associate Director of the Statistical Consulting Service in the Department of Statistics at Purdue University. His research interests include statistical modeling for improved control of complex engineering systems, Bayesian data analysis, experimental design, and causal inference. Specific major objectives of his current research include the development of Bayesian and machine learning algorithms for control of cyber-physical additive manufacturing systems, the design of multi-armed bandit algorithms, propensity score methodology for Big Data, and causal inference in the presence of principal strata. He received his Masters and PhD in Statistics from Harvard University.

Dr Wenzhuo Wu is the Ravi and Eleanor Talwar Rising Star Assistant Professor in School of Industrial Engineering at Purdue University. He received his BS in Electronic Information Science and Technology in 2005 from the University of Science and Technology of China (USTC), Hefei and his ME in Electrical and Computer Engineering from the National University of Singapore (NUS) in 2008. Dr Wu received his PhD from Georgia Institute of Technology in Materials Science and Engineering in 2013. Dr Wu's research interests include design, manufacturing, and integration of 1D and 2D nanomaterials for applications in energy, electronics, optoelectronics, and wearable devices. He was a recipient of the Oak Ridge Associated Universities (ORAU) Ralph E. Powe Junior Faculty Enhancement Award in 2016, and the IOP Semiconductor Science and Technology Best Early Career Research in 2017.